RSC Advances

PAPER

Cite this: *RSC Adv.*, 2023, **13**, 15410

Facile formation of barium titanium oxyhydride on a titanium hydride surface as an ammonia synthesis catalyst†

Yoshihiro Goto, *[a] Masashi Kikugawa,[a] Keisuke Kobayashi, [b] Yuichi Manaka, [b] Tetsuya Nanba,[b] Hideyuki Matsumoto,[bc] Mitsuru Matsumoto,[a] Masakazu Aoki[a] and Haruo Imagawa [a]

Oxyhydrides are promising compounds as supports for ammonia synthesis catalysts because they suppress hydrogen poisoning on the catalyst surface and enhance the ammonia synthesis activity. Herein, we developed a facile method for preparing $BaTiO_{2.5}H_{0.5}$, a perovskite oxyhydride, on a TiH_2 surface *via* the conventional wet impregnation method using TiH_2 and Ba hydroxide. Scanning electron microscopy and high-angle annular dark-field scanning transmission electron microscopy observations revealed that $BaTiO_{2.5}H_{0.5}$ crystallized as nanoparticles of *ca.* 100–200 nm on the TiH_2 surface. The Ru-loaded catalyst Ru/$BaTiO_{2.5}H_{0.5}$-TiH_2 exhibited 2.46 times higher ammonia synthesis activity (3.05 mmol-NH_3 g^{-1} h^{-1} at 400 °C) than the benchmark Ru catalyst Ru–Cs/MgO (1.24 mmol-NH_3 g^{-1} h^{-1} at 400 °C) because of the suppression of hydrogen poisoning. The analysis of reaction orders showed that the effect of suppressing hydrogen poisoning on Ru/$BaTiO_{2.5}H_{0.5}$-TiH_2 was equivalent to that of the reported Ru/$BaTiO_{2.5}H_{0.5}$ catalyst, thus supporting the formation of $BaTiO_{2.5}H_{0.5}$ perovskite oxyhydride. This study demonstrated that the selection of appropriate raw materials facilitates the formation of $BaTiO_{2.5}H_{0.5}$ oxyhydride nanoparticles on the TiH_2 surface using the conventional synthesis method.

Received 8th March 2023
Accepted 17th May 2023

DOI: 10.1039/d3ra01539d

rsc.li/rsc-advances

Introduction

Ammonia (NH_3), an essential raw material in the production of agricultural fertilizers and synthetic chemicals, has recently attracted attention owing to its applicability as a hydrogen carrier or fuel.[1,2] Ammonia is predominantly produced *via* the Haber–Bosch (HB) process, which accounts for 1–2% of the global energy demand and 2.5% of global CO_2 emissions.[3] Most of the CO_2 emissions are responsible for hydrogen production processes using steam reforming ($CH_4 + H_2O \rightarrow CO + 3H_2$) and water gas shift reactions ($CO + H_2O \rightarrow CO_2 + H_2$). Replacing these processes with water electrolysis ($2H_2O \rightarrow 2H_2 + O_2$) using renewable energy can significantly reduce this CO_2 emission.[4] However, renewable electricity sources of an intermittent nature are not compatible with ammonia synthesis *via* the conventional HB process[5] because the process is operated on large-scale and steady-state operations. On this basis, ammonia synthesis catalysts need severe reaction conditions (at 450–600 °C and 15–40 MPa).[5] Therefore, ammonia synthesis catalysts that work under mild conditions should be developed for ammonia synthesis using renewable electricity sources.

The rate-determining step in the synthesis of ammonia ($3H_2 + N_2 \rightarrow 2NH_3$) is the dissociation of the N_2 triple bond (945 KJ mol^{-1}), which is the strongest bond among those in diatomic molecules.[6,7] Supported ruthenium (Ru) catalysts are the most promising candidates for ammonia synthesis under mild conditions because optimum N_2 adsorption energy facilitates N_2 dissociation on the Ru surface.[8] Strongly basic supports (such as CeO_2, $La_{0.5}Pr_{0.5}O_{1.75}$, Ba/$Ce_{0.5}La_{0.5}O_{1.75}$, CeO_2-PrO_x, and $Ce_{0.5}La_{0.5-x}Ti_xO_{1.75+0.5x}$)[9–14] further promote N_2 dissociation because the basic compounds enhance the electron transfer from the Ru metal to the antibonding orbital of N_2.[15] However, hydrogen atoms generated by H_2 dissociation are often adsorbed on the active sites of the Ru surface, thereby preventing N_2 dissociation on the Ru surface.[16] In recent years, oxyhydrides such as $BaTiO_{3-x}H_x$, $BaCeO_{3-x}H_yN_z$, $LaH_{3-2x}O_x$, GdHO, and SmHO have been reported as supports that suppress hydrogen poisoning and enhance the ammonia synthesis activity of Ru catalysts.[17–20] Suppression of hydrogen poisoning is presumed to originate from the diffusivity of hydride (H^-), which allows hydrogen spillover from the Ru metal to the surface of the oxyhydride supports.[21]

---

[a] Toyota Central R&D Labs., Inc., 41-1 Yokomichi, Nagakute 480-1192, Aichi, Japan. E-mail: yoshihiro-goto@mosk.tytlabs.co.jp

[b] Renewable Energy Research Center, National Institute of Advanced Industrial Science and Technology, 2-2-9 Machiikedai, Koriyama 963-0298, Fukushima, Japan

[c] Department of Chemical Science and Engineering, School of Materials and Chemical Technology, Tokyo Institute of Technology, 2-12-1 Ookayama, Meguro-ku, Tokyo, 152-8552, Japan

† Electronic supplementary information (ESI) available. See DOI: **https://doi.org/10.1039/d3ra01539d**

Transition-metal (TM) oxyhydride synthesis is generally complicated because the differences in chemical properties (such as reactivity, volatility, and ionic radius) among anions prevent different anions in an identical compound from becoming stable.[22] For this reason, solid-state topochemical reactions and/or high-pressure reactions have been used to synthesize TM oxyhydrides.[22] $BaTiO_{3-x}H_x$, which is a promising TM perovskite oxyhydride support for ammonia synthesis catalysts, cannot be prepared by simply reducing $BaTiO_3$ with hydrogen. However, this oxyhydride is accessible *via* a solid-state topochemical reaction involving $BaTiO_3$ and CaH_2 because the reaction can provide a metastable phase by exchanging the oxide (O^{2-}) in $BaTiO_3$ with hydride (H^-) in CaH_2 while maintaining the basic framework structure of $BaTiO_3$.[23] However, materials preparation using the topochemical reaction is not suitable for practical use because the reaction involves a multi-step process: (1) mixing $BaTiO_3$ and the moisture-sensitive CaH_2 in an inert atmosphere, (2) calcining the mixture for a week under vacuum, and (3) washing in an inert atmosphere to extract product $BaTiO_{3-x}H_x$ by removing the residual CaH_2 and by-product CaO. The practical utility of $BaTiO_{3-x}H_x$ may be limited by low producibility owing to the multi-step process. Thus, developing more facile, efficient ways to prepare $BaTiO_{3-x}H_x$ is necessary to accelerate the application of $BaTiO_{3-x}H_x$. Moreover, the development can lead to the discovery of novel oxyhydrides.

Recently, Uchimura *et al.*[24] have reported the direct synthesis of $BaTiO_{3-x}H_x$ by a mechanochemical method using BaH_2, BaO, and TiO_2 and confirmed its performance as a hydrogen-permeable electrode. However, handling in an inert atmosphere is still required because BaH_2 and BaO are sensitive to moisture. Herein, we demonstrated the synthesis of $BaTiO_{3-x}H_x$ ($x = 0.5$), a perovskite oxyhydride, on a TiH_2 surface *via* conventional wet impregnation method using TiH_2 and $Ba(OH)_2 \cdot 8H_2O$, which are stable in moisture and air. The obtained $BaTiO_{2.5}H_{0.5}$ was crystallized as fine particles of 100–200 nm size that covered the TiH_2 particle surface. The Ru-loaded catalyst, Ru/$BaTiO_{2.5}H_{0.5}$-TiH_2, showed 2.46 times higher ammonia synthesis activity than Ru–Cs/MgO as benchmark Ru catalyst. Moreover, Ru/$BaTiO_{2.5}H_{0.5}$-TiH_2 suppressed hydrogen poisoning, thereby proving the formation of $BaTiO_{2.5}H_{0.5}$ perovskite oxyhydride.

Methods

$BaTiO_{2.5}H_{0.5}$-TiH_2 was synthesized *via* the wet impregnation method using TiH_2 powder and Ba hydroxide solution. TiH_2 (98%, −325 mesh, Sigma-Aldrich) was impregnated with a solution containing the desired amount of $Ba(OH)_2 \cdot 8H_2O$ (98.0%, FUJIFILM Wako Chemicals) dissolved in 3 : 2 (v/v) H_2O/ethanol at 230 °C in the air, after which it was heated at 350 °C for 3 h in a 10% H_2/N_2 atmosphere. The Ba addition amounts were varied from 0–15 wt% on a $Ba(OH)_2$ basis. The obtained compounds are hereafter referred to as Ba(α)-TiH_2 (α: wt% of $Ba(OH)_2$). Reference compounds Ba(α)-TiO_2 (where α = wt% of $Ba(OH)_2$) were prepared using the same protocols as for Ba(α)-TiH_2, except TiO_2 (99.9%, Rutile, Sigma-Aldrich) was used instead of TiH_2. Ba(10)-TiH_2 synthesized using $Ba(CH_3COO)_2$ (99.0%, FUJIFILM Wako Chemicals) or $Ba(NO_3)_2$ (99.0%, FUJIFILM Wako Chemicals) instead of $Ba(OH)_2 \cdot 8H_2O$ were also prepared to investigate the effect of Ba sources. Cs/MgO as a benchmark compound was prepared by impregnation using MgO (99%, Sigma-Aldrich) and Cs_2CO_3 (99.9%, Sigma-Aldrich)/ethanol solution, followed by thermal treatment at 350 °C for 3 h under 10% H_2/N_2. Ru-loaded catalysts, such as Ru/Ba(α)-TiH_2, Ru/Ba(α)-TiO_2, and Ru–Cs/MgO, were prepared by impregnation using $Ru_3(CO)_{12}$ (99%, Sigma-Aldrich)/tetrahydrofuran solution. The suspension was stirred for 5 h, and the solvent was subsequently evaporated at 27 °C. The obtained compound was dried at 80 °C for 16 h in the air. The Cs and Ru loading amounts were 1 wt% on a metal basis.

X-ray diffraction (XRD) patterns and were collected at room temperature using SmartLab (Rigaku) with Cu Kα radiation (λ = 1.54056 Å). The obtained XRD patterns were analyzed using the JANA2006 software.[25] The neutron diffraction (ND) pattern was collected at room temperature using the NOVA time-of-flight (TOF) neutron diffractometer at the J-PARC facility in Japan. The obtained ND pattern was analyzed using Z-Rietveld software.[26] Fourier-transform infrared (FT-IR) spectra were recorded using an iS50 spectrometer (Thermo Fisher) equipped with a diffuse reflectance optics accessory. Samples were pretreated at 200 °C for 30 min in flowing He and then examined at 50 °C. Scanning electron microscopy (SEM) images were obtained using a JSM-7400F (JEOL) and a SU3500 (Hitachi) operated at 1.5 kV. High-angle annular dark-field scanning transmission electron microscopy (HAADF-STEM) and energy-dispersive X-ray spectroscopy (EDS) mapping images were obtained using a Tecnai Osiris (FEI) operated at 200 kV. X-ray photoelectron spectroscopy (XPS) was conducted on a Quantera SXM instrument (ULVAC PHI) using Al Kα radiation (1486.6 eV). CO amounts adsorbed by the catalyst were estimated using a BEL-METAL-3 (MicrotracBEL). CO pulse injections (1.99% CO/He) to the samples were conducted at 50 °C after the pretreatment at 400 °C for 2 h in 100% H_2.

The ammonia synthesis activities under ambient pressure were estimated using a fixed-bed reactor connected to mass flow controllers. A sample (0.2 g) was suspended on a bed of quartz wool in a quartz tube and preheated at 400 °C for 2 h in 75% H_2/N_2 ($H_2/N_2 = 3$) at a flow rate of 80 mL min^{-1}. The activity measures were conducted at 300–400 °C in 75% H_2/N_2 ($H_2/N_2 = 3$) at a flow rate of 80 mL min^{-1}. The ammonia concentrations in the outlet of the quartz tube were monitored by FT-IR spectroscopy and converted into ammonia synthesis rates. Reaction orders of ammonia synthesis with respect to H_2, N_2, and NH_3 were estimated using the method of Aika *et al.*[27]

Results and discussion

The XRD patterns of Ba(α)-TiH_2 (α = 0, 1, 3, 5, 10, and 15) predominantly showed the cubic phase of the fluorite structure ($Fm\bar{3}m$) with the lattice parameter of a = 4.4489–4.4519 Å (Fig. 1). The lattice parameter matches that of the reported TiH_2 (a = 4.4512(1) Å),[28] showing that the cubic phase is TiH_2. The XRD patterns of samples with α = 0 and 1 only showed the

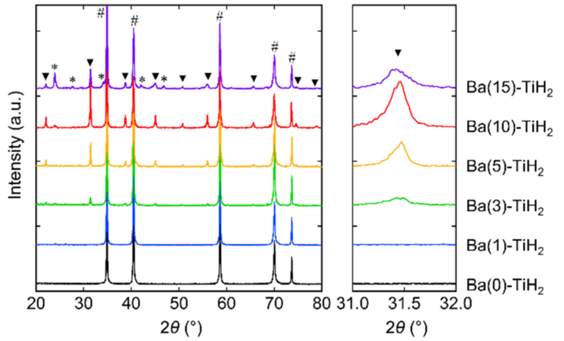

Fig. 1 XRD patterns of Ba(α)-TiH$_2$ ($\alpha = 0, 1, 3, 5, 10,$ and 15). Hashtags (#), triangles (▼), and asterisks (*) indicate peaks arising from TiH$_2$, BaTiO$_{2.5}$H$_{0.5}$, and BaCO$_3$, respectively.

single phase of TiH$_2$, whereas the XRD patterns of $\alpha \geq 3$ samples contained an additional cubic phase of perovskite structure ($Pm\bar{3}m$; Fig. S1 in the ESI†). The lattice volume was estimated to be $V = 64.926$–65.073 Å^3 (Table 1), which approaches that reported for cubic BaTiO$_{2.38}$H$_{0.62}$ perovskite oxyhydride ($Pm\bar{3}m$, $V = 65.140$ Å^3)[23] rather than tetragonal BaTiO$_3$ perovskite oxide ($P4mm$, $V = 64.281$ Å^3),[29] which indicates that the additional cubic phase is BaTiO$_{3-x}$H$_x$ perovskite oxyhydride. The H content x in BaTiO$_{3-x}$H$_x$ ($\alpha = 3, 5, 10,$ and 15) were determined to be $x = 0.47$–0.57 based on Vegard's law (Table 1; hereafter, the obtained perovskite oxyhydride is referred to as BaTiO$_{2.5}$H$_{0.5}$). The formation of oxygen-deficient BaTiO$_{3-\delta}$ is unlikely because the lattice volume of BaTiO$_{2.5}$H$_{0.5}$ ($V = 64.926$–65.073 Å^3) is larger than that reported for cubic BaTiO$_{3-\delta}$ perovskite oxide ($\delta = 0.25$, $Pm\bar{3}m$, $V = 64.337$ Å^3) where the lattice volume does not change through the formation of oxygen defects.[30] The formation of the BaTiO$_{3-\delta}$(OH)$_\delta$ oxyhydroxide through OH$^-$ incorporation is also denied because no peaks associated with OH bonds (observed at 3400 cm^{-1} in BaTiO$_3$ system)[31] were observed by FT-IR spectroscopy (Fig. S2†). Moreover, the XRD patterns of the $\alpha = 10$ and 15 samples showed that BaCO$_3$ can potentially form through the reaction of unreacted Ba(OH)$_2$ with atmospheric CO$_2$ absorbed during impregnation. Thus, the addition of Ba into TiH$_2$ forms BaTiO$_{2.5}$H$_{0.5}$ perovskite oxyhydride and BaCO$_3$.

Table 1 Physical characteristics of Ba(α)-TiH$_2$ ($\alpha = 0, 1, 3, 5, 10,$ and 15)

Sample	Lattice volume of BaTiO$_{3-x}$H$_x$^{a} (Å^3)	H content x^b
Ba(0)-TiH$_2$	—	—
Ba(1)-TiH$_2$	—	—
Ba(3)-TiH$_2$	65.002(2)	0.52
Ba(5)-TiH$_2$	64.926(2)	0.47
Ba(10)-TiH$_2$	65.009(2)	0.56
Ba(15)-TiH$_2$	65.073(3)	0.57

[a] Calculated from the lattice parameters based on the cubic perovskite structure ($Pm\bar{3}m$, $Z = 1$). [b] Determined from Vegard's law using the lattice volumes of BaTiO$_3$ ($V = 64.281$ Å^3)[29] and BaTiO$_{2.38}$H$_{0.62}$ ($V = 65.140$ Å^3).[23]

The ND pattern of Ba(10)-TiH$_2$ was collected to investigate the presence of the hydride in BaTiO$_{2.5}$H$_{0.5}$ (Fig. S3 and Table S1†). Rietveld refinement was performed by assuming that the secondary phase is a BaTiO$_{3-x}$H$_x$ cubic perovskite with a $Pm\bar{3}m$ structural model, where Ba, Ti, and O/H atoms are placed at the Wyckoff position of 1a (0, 0, 0), 1b (0.5, 0.5, 0.5), and 3c (0, 0.5, 0.5), respectively. Cubic TiH$_2$ ($Fm\bar{3}m$) was added as a primary phase. Refinement converged to O and H occupancies of $g(\mathrm{O}) = 0.886(2)$ and $g(\mathrm{H}) = 0.114(2)$, which yields the BaTiO$_{2.658(6)}$H$_{0.342(6)}$ composition and supports the notion that perovskite phase contains hydride. We note here that the difference in the neutron scattering lengths of oxygen and hydrogen (O: 5.803 fm, H: −3.741 fm)[32] gives the composition BaTiO$_{2.438(6)}$ when the refinement is performed by assuming that the secondary phase is oxygen-deficient BaTiO$_{3-\delta}$. However, because the formation of oxygen-deficient BaTiO$_{3-\delta}$ is ruled out by considering the lattice volumes estimated by the XRD analysis, the ND results support the formation of an oxyhydride.

The degrees of BaTiO$_{2.5}$H$_{0.5}$ and BaCO$_3$ formation were determined by Rietveld refinement of the XRD patterns of Ba(α)-TiH$_2$. We note here that components (less than about 1%) that are not detected in the XRD analysis are not considered. As shown in Fig. 2, the mass fraction of BaTiO$_{2.5}$H$_{0.5}$ is 0% at $0 \leq \alpha \leq 1$ and higher at $3 \leq \alpha \leq 10$ (1.6% to 8.7%). However, a lower fraction was observed at $\alpha = 15$ (4.5%). The addition of Ba to TiH$_2$ facilitates the formation of BaTiO$_{2.5}$H$_{0.5}$, while excess Ba inhibits its formation. Thus, the optimum amount of Ba(OH)$_2$ needed to form BaTiO$_{2.5}$H$_{0.5}$ corresponds to $\alpha = 10$. The mass fraction of the formed BaCO$_3$ was 0% at $0 \leq \alpha \leq 5$ but higher at $10 \leq \alpha \leq 15$ (0.7 to 4.3%), which implies that unreacted Ba(OH)$_2$ remains at $\alpha \geq 10$. The samples also exhibited colors that depend on the amounts of BaTiO$_{2.5}$H$_{0.5}$ and BaCO$_3$ amounts (Fig. S4†). Ba(0)-TiH$_2$ and Ba(5)-TiH$_2$ are gray, which is typical of TiH$_2$, while Ba(10)-TiH$_2$ is dark blue, which is typical of BaTiO$_{2.5}$H$_{0.5}$,[23] which also supports the notion that the BaTiO$_{2.5}$H$_{0.5}$ perovskite oxyhydride had formed. Ba(15)-TiH$_2$ is brown, which is possibly due to mixed colors associated with TiH$_2$, BaTiO$_{2.5}$H$_{0.5}$, and BaCO$_3$.

The SEM image of Ba(0)-TiH$_2$ revealed that the particle size of TiH$_2$ ranged from several to tens of μm (Fig. S5 and S6†). Particle size was not affected by the amount of added Ba, which

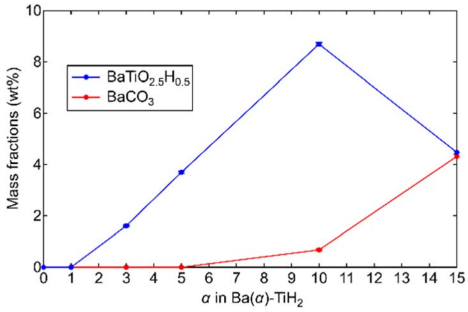

Fig. 2 Mass fractions of BaTiO$_{2.5}$H$_{0.5}$ and BaCO$_3$ in Ba(α)-TiH$_2$ determined by Rietveld refinements of the XRD patterns of Ba(α)-TiH$_2$. Cubic TiH$_2$ ($Fm\bar{3}m$), cubic BaTiO$_{2.5}$H$_{0.5}$ ($Pm\bar{3}m$), and orthorhombic BaCO$_3$ ($Pnma$) phases were applied during the analysis.

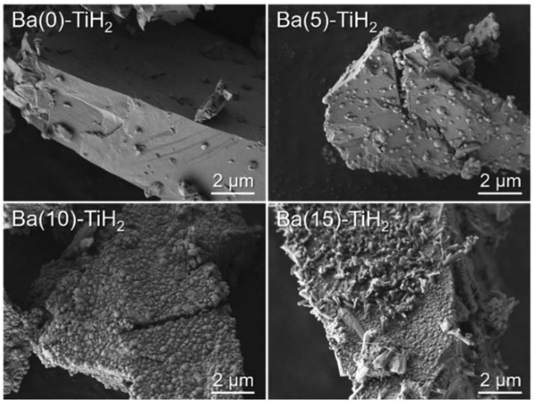

Fig. 3 SEM images of Ba(α)-TiH$_2$ (α = 0, 5, 10, and 15) at 100 00× magnification.

agreed with the identical specific surface area of Ba(α)-TiH$_2$ ($0 \leq \alpha \leq 15$; 1.65–1.91 m^2 g^{-1}). The particle surface of Ba(0)-TiH$_2$ and Ba(1)-TiH$_2$ were relatively smooth; by comparison, nanoparticles of *ca.* 100–200 nm were dispersed on the TiH$_2$ surface of Ba(3)-TiH$_2$ and Ba(5)-TiH$_2$ (Fig. 3). The nanoparticles were expected to be $BaTiO_{2.5}H_{0.5}$ because $BaTiO_{2.5}H_{0.5}$ in addition to TiH$_2$ was observed in the XRD patterns of Ba(3)-TiH$_2$ and Ba(5)-TiH$_2$ (Fig. 1). The EDX mappings in the HAADF-STEM image of Ru/Ba(5)-TiH$_2$ show that Ba and O elements were localized at the nanoparticles (Fig. 4), thus supporting the identification of the nanoparticles as $BaTiO_{2.5}H_{0.5}$. The Ba/Ti atomic ratio estimated from the XPS analysis was higher than that of the feed ratio in the preparation, also supporting that the nanoparticles are $BaTiO_{2.5}H_{0.5}$. The SEM image of Ba(10)-TiH$_2$ showed that the $BaTiO_{2.5}H_{0.5}$ nanoparticles fully covered the TiH$_2$ particle. Moreover, the SEM image of Ba(15)-TiH$_2$ showed needle-shaped particles on the $BaTiO_{2.5}H_{0.5}$ nanoparticles. The crystals were identified as BaCO$_3$ according to the XRD pattern because BaCO$_3$ generally formed needle-shape crystals.[33] Therefore, $BaTiO_{2.5}H_{0.5}$ was formed as 100–200 nm nanoparticles at $\alpha \geq 3$, and BaCO$_3$ was formed as needle shape particles at $\alpha \geq 10$ (Fig. 5).

The XRD patterns of Ba(α)-TiO$_2$ (α = 0, 5, 10, 15) synthesized as comparison are shown in Fig. S8.† All samples showed predominantly rutile TiO$_2$. Ba(0)-TiO$_2$ was the single phase of TiO$_2$, whereas Ba(α)-TiO$_2$ (α = 5, 10, and 15) contained additional Ba$_2$TiO$_4$ and BaCO$_3$. The cubic phase of $BaTiO_{2.5}H_{0.5}$ formed in Ba(α)-TiH$_2$ was not observed with the addition of any amount of Ba(OH)$_2$. Therefore, TiH$_2$ is essential for $BaTiO_{2.5}H_{0.5}$ formation.

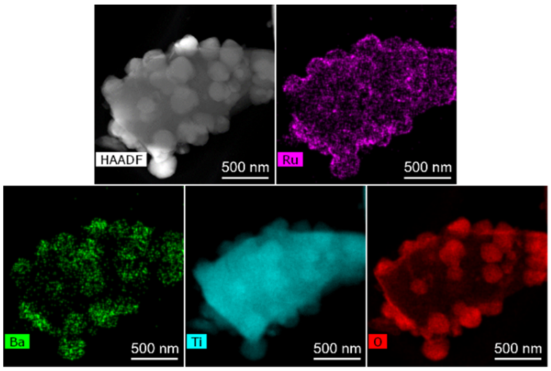

Fig. 4 STEM-HAADF and EDX mapping images of Ru/Ba(5)-TiH$_2$.

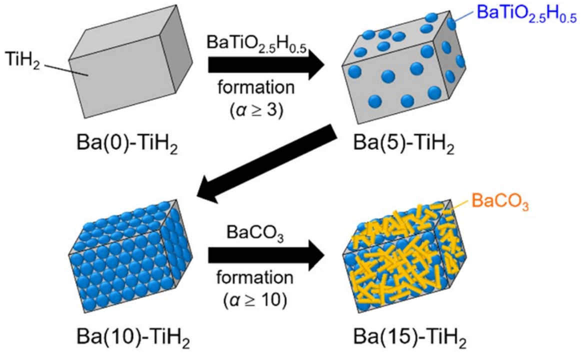

Fig. 5 Images of the morphological change of Ba(α)-TiH$_2$.

How is TiH$_2$ involved in the formation of $BaTiO_{2.5}H_{0.5}$? TiH$_2$ consumed to form $BaTiO_{2.5}H_{0.5}$ is calculated to be 2.1% for Ba(10)-TiH$_2$ which contains the highest amount of $BaTiO_{2.5}H_{0.5}$ (8.7%; Fig. 2), suggesting that only the surface part of the TiH$_2$ particles contributes to the formation. This is supported by the SEM and TEM observations (Fig. 3 and 4). Because metal hydrides are generally unstable in an oxidizing atmosphere, the surface of TiH$_2$ particles is known to be covered by an oxide film of TiO$_2$.[34] TiH$_2$ (Ti^{2+}) partially oxidized to TiO$_2$ (Ti^{4+}) possibly contributes to the formation of $BaTiO_{2.5}H_{0.5}$ (Ti$^{3.5+}$) *via* the reaction $Ba(OH)_2 + 0.5x TiH_2 + (1 - 0.5x)TiO_2 \rightarrow BaTiO_{3-x}H_x + H_2O$. Moreover, the effect of Ba reagents on $BaTiO_{2.5}H_{0.5}$ formation was investigated. The XRD patterns of Ba(10)-TiH$_2$ synthesized using Ba(CH$_3$COO)$_2$ or Ba(NO$_3$)$_2$ instead of $Ba(OH)_2 \cdot 8H_2O$ are shown in Fig. S9.† The XRD pattern of Ba(10)-TiH$_2$ synthesized *via* Ba(CH$_3$COO)$_2$ showed only TiH$_2$ and Ba(CH$_3$COO)$_2$ and no formation of $BaTiO_{2.5}H_{0.5}$. While Ba(10)-TiH$_2$ synthesized *via* Ba(NO$_3$)$_2$ contained $BaTiO_{2.5}H_{0.5}$, its mass fraction (1.5%) was only 0.17-times that of the Ba(10)-TiH$_2$ synthesized *via* $Ba(OH)_2 \cdot 8H_2O$ (8.7%). These observations suggest that the hydroxide ion (OH$^-$) promotes the formation of $BaTiO_{2.5}H_{0.5}$.

The ammonia synthesis activities of Ru/Ba(α)-TiH$_2$ ($0 \leq \alpha \leq 15$) catalysts were examined at 300–400 °C under ambient pressure (Fig. 6a). Ammonia synthesis rates of all catalysts increased at elevated temperature. Ru/Ba(0)-TiH$_2$ exhibited ammonia synthesis activity at ≥375 °C. The ammonia synthesis rate of Ru/Ba(0)-TiH$_2$ (0.05 mmol g^{-1} h^{-1} at 400 °C) was 0.04 times that of Ru/Cs–MgO (1.24 mmol g^{-1} h^{-1} at 400 °C), which was often called as benchmark Ru catalysts.[35,36] The activity of Ru/Ba(1)-TiH$_2$ (0.20 mmol g^{-1} h^{-1} at 400 °C) was higher than that of Ru/Ba(0)-TiH$_2$ but remained lower than that of Ru/Cs–MgO. However, by contrast, the activities of Ru/Ba(3)-TiH$_2$, Ru/Ba(5)-TiH$_2$, and Ru/Ba(10)-TiH$_2$ (1.73, 2.08, and 3.05 mmol g^{-1} h^{-1} at 400 °C, respectively) were higher than that of Ru–Cs/MgO by a factor of 1.40, 1.68, and 2.46, respectively. Activity increased

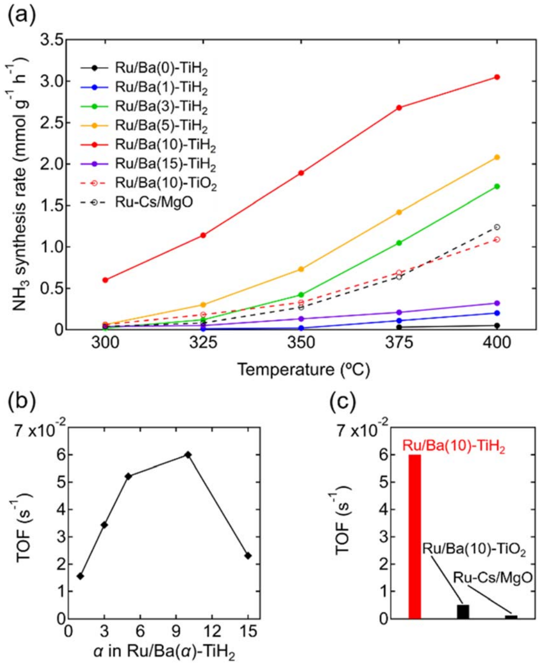

Fig. 6 (a) Temperature dependence of the NH_3 synthesis rates for Ru/Ba(α)-TiH_2 (α = 0, 1, 3, 5, 10, and 15), Ru/Ba(10)-TiO_2, and Ru–Cs/MgO (reaction conditions: catalyst, 0.2 g; reaction gas, $H_2/N_2 = 3$ at a flow rate of 80 mL min^{-1}; pressure = ambient pressure). (b) TOF of Ru/Ba(α)-TiH_2 (α = 0, 1, 3, 5, 10, and 15) at 350 °C as functions of $Ba(OH)_2$ added amount α. (c) TOF of Ru/Ba(10)-TiH_2, Ru/Ba(10)-TiO_2, and Ru–Cs/MgO at 350 °C.

with the increase in Ba addition amount in $0 \leq \alpha \leq 10$, whereas the activity decreased at $\alpha = 15$ (0.32 mmol g^{-1} h^{-1} at 400 °C). Therefore, the most active catalyst among Ru/Ba(α)-TiH_2 ($0 \leq \alpha \leq 15$) was Ru/Ba(10)-TiH_2. The activity of Ru/Ba(10)-TiH_2 was higher than that of Ru/Ba(10)-TiO_2 (1.09 mmol g^{-1} h^{-1} at 400 °C), thereby suggesting that $BaTiO_{2.5}H_{0.5}$ formation was responsible for the high activity of Ru/Ba(10)-TiH_2.

The TOF for the ammonia synthesis reaction at 350 °C was estimated to obtain a deeper insight into the correlation between ammonia synthesis activity and catalyst composition. As shown in Fig. 6b, the TOF of Ru/Ba(α)-TiH_2 increased with increasing amount of Ba addition at $1 \leq \alpha \leq 10$ (1.56×10^{-2} s^{-1} to 6.00×10^{-2} s^{-1}) but decreased at $\alpha = 15$ (2.31×10^{-2} s^{-1}). This trend was consistent with the trend of the mass fraction of $BaTiO_{2.5}H_{0.5}$ (Fig. 2); these observations support that $BaTiO_{2.5}H_{0.5}$ formation contributes to the increase in ammonia synthesis activity. This was supported by the fact that the TOF of Ru/Ba(10)-TiH_2 (6.00×10^{-2} s^{-1}) was 12 and 46 times larger than those of Ru/Ba(10)-TiO_2 (0.51×10^{-2} s^{-1}) and Ru–Cs/MgO (0.13×10^{-2} s^{-1}), respectively (Fig. 6c). Interestingly, the TOF of Ru/Ba(15)-TiH_2 (2.31×10^{-2} s^{-1}) was lower than that of Ru/Ba(5)-TiH_2 (5.21×10^{-2} s^{-1}) despite the higher mass fraction of $BaTiO_{2.5}H_{0.5}$ for Ru/Ba(15)-TiH_2 (4.48%) than that for Ru/Ba(5)-TiH_2 (3.70%). The formation of $BaCO_3$, which partially covered the $BaTiO_{2.5}H_{0.5}$ particles (Fig. 3), was expected to inhibit the ammonia synthesis reaction of Ru/Ba(15)-TiH_2 because $BaCO_3$ was stable in the reaction temperature.[37]

Table 2 Reaction orders[a] for ammonia synthesis reaction over Ru/Ba(10)-TiH_2 and Ru–Cs/MgO

	Order		
Catalyst	H_2	N_2	NH_3
Ru/Ba(10)-TiH_2	0.15	0.79	−0.36
Ru–Cs/MgO	−0.59	0.89	0.11

[a] Estimated from results of kinetic analysis shown in Fig. S8.

Finally, reaction orders with respect to H_2, N_2 and NH_3 were investigated using the method of Aika *et al.*[27] (Fig. S10 and Table S3†). The H_2 order of Ru/Ba(10)-TiH_2 (0.15) was higher than that of Ru–Cs/MgO (−0.59), reflecting that compared to Ru–Cs/MgO, Ru/Ba(10)-TiH_2 had less hydrogen poisoning, which prevented N_2 dissociation on Ru (Table 2).[16] The low hydrogen poisoning effect allowed Ru/Ba(10)-TiH_2 to exhibit higher ammonia synthesis activity than Ru–Cs/MgO. The N_2 orders of Ru/Ba(10)-TiH_2 (0.79) and Ru–Cs/MgO (0.89) were virtually coincident, reflecting that the rate-determining step for both catalysts was the unimolecular cleavage reaction of N_2 for both catalysts. Moreover, the orders of Ru/Ba(10)-TiH_2 (H_2 order: 0.15, N_2 order: 0.79) agreed well with the reported orders of Ru/$BaTiO_{2.5}H_{0.5}$ (H_2 order: 0.2, N_2 order: 0.7).[17] Because Ru/$BaTiO_3$, the reference catalyst for Ru/$BaTiO_{2.5}H_{0.5}$, exhibits stronger hydrogen poisoning due to the absence of hydride in the support perovskite (H_2 order: −0.89, N_2 order: 1.2),[17] the agreement of the H_2 and N_2 orders between Ru/Ba(10)-TiH_2 and Ru/$BaTiO_{2.5}H_{0.5}$ supports the formation of $BaTiO_{2.5}H_{0.5}$ in Ru/Ba(10)-TiH_2. The NH_3 order of Ru/Ba(10)-TiH_2 (−0.36) was higher than that reported for Ru/$BaTiO_{2.5}H_{0.5}$ (−0.64), indicating that the ammonia decomposition reaction on Ru/Ba(10)-TiH_2 was relatively inhibited. The inhibition may be attributed to the reaction pressure of this study (ambient pressure) being lower than that of reported Ru/$BaTiO_{2.5}H_{0.5}$ (5 MPa) because the ammonia decomposition reaction generally proceeded at a higher pressure.[38]

Conclusions

The selection of appropriate raw materials allowed for $BaTiO_{2.5}H_{0.5}$ perovskite oxyhydride nanoparticles to be formed on the TiH_2 surface through the conventional wet impregnation method. $BaTiO_{2.5}H_{0.5}$ crystallized as *ca.* 100–200 nm sized nanoparticles on the surface of TiH_2. Hydroxide in $Ba(OH)_2$ involved $BaTiO_{2.5}H_{0.5}$ formation. Ru-loaded catalysts inhibited hydrogen poisoning and showed higher ammonia synthesis activity compared to that of the Ru–Cs/MgO benchmark catalyst. We believe that further investigation of oxyhydride prepared *via* the wet impregnation method accelerates the use of oxyhydride as ammonia synthesis catalysts.

Author contributions

Yoshihiro Goto: conceptualization, investigation, writing – original draft, Masashi Kikugawa: investigation, Keisuke

Kobayashi: data curation, Yuichi Manaka: validation, Tetsuya Nanba: conceptualization, project administration, Hideyuki Matsumoto: formal analysis Mitsuru Matsumoto: validation, Masakazu Aoki: supervision, project administration, Haruo Imagawa: supervision, writing-review &editing.

Conflicts of interest

There are no conflicts to declare.

Acknowledgements

The authors acknowledge Mr Akira Takatsuki (National Institute of Advanced Industrial Science and Technology, Ibaraki, Japan) for his contribution in collecting the SEM and STEM-HAADF images.

Notes and references

1 J. W. Erisman, M. A. Sutton, J. Galloway, Z. Klimont and W. Winiwarter, *Nat. Geosci.*, 2008, **1**, 636.
2 A. Klerke, C. H. Christensen, J. K. Nørskov and T. Vegge, *J. Mater. Chem.*, 2008, **18**, 2304.
3 P. H. Pfromm, *J. Renewable Sustainable Energy*, 2017, **9**, 034702.
4 C. Smith, A. K. Hill and L. Torrente-Murciano, *Energy Environ. Sci.*, 2020, **13**, 331.
5 M. Ravi and J. W. Makepeace, *Chem. Sci.*, 2022, **13**, 890.
6 S. Gambarotta and J. Scott, *Angew. Chem., Int. Ed.*, 2004, **43**, 5298.
7 K. Honkala, A. Hellman, I. N. Remediakis, A. Logadottir, A. Carlsson, S. Dahl, C. H. Christensen and J. K. Nørskov, *Science*, 2005, **307**, 555.
8 C. J. H. Jacobsen, S. Dahl, B. S. Clausen, S. Bahn, A. Logadottir and J. K. Nørskov, *J. Am. Chem. Soc.*, 2001, **123**, 8404.
9 Y. Niwa and K. Aika, *Chem. Lett.*, 1996, **3**, 3.
10 Y. Ogura, K. Tsujimaru, K. Sato, S. Miyahara, T. Toriyama, T. Yamamoto, S. Matsumura and K. Nagaoka, *ACS Sustainable Chem. Eng.*, 2018, **6**, 17258.
11 Y. Ogura, K. Sato, S. Miyahara, Y. Kawano, T. Toriyama, T. Yamamoto, S. Matsumura, S. Hosokawa and K. Nagaoka, *Chem. Sci.*, 2018, **9**, 2230.
12 K. Sato, S. Miyahara, Y. Ogura, K. Tsujimaru, Y. Wada, T. Toriyama, T. Yamamoto, S. Matsumura and K. Nagaoka, *ACS Sustainable Chem. Eng.*, 2020, **8**, 2726.
13 M. Kikugawa, Y. Goto, K. Kobayashi, T. Nanba, H. Matsumoto and H. Imagawa, *J. Catal.*, 2022, **413**, 934.
14 Y. Goto, M. Kikugawa, K. Kobayashi, T. Nanba, H. Matsumoto and H. Imagawa, *Chem. Commun.*, 2022, **58**, 3210.
15 K. Aika, A. Ohya, A. Ozaki, Y. Inoue and I. Yasumori, *J. Catal.*, 1985, **92**, 305.
16 Y. Kadowaki and K. Aika, *J. Catal.*, 1996, **161**, 178.
17 Y. Tang, Y. Kobayashi, N. Masuda, Y. Uchida, H. Okamoto, T. Kageyama, S. Hosokawa, F. Loyer, K. Mitsuhara, K. Yamanaka, Y. Tamenori, C. Tassel, T. Yamamoto, T. Tanaka and H. Kageyama, *Adv. Energy Mater.*, 2018, **8**, 1801772.
18 M. Kitano, J. Kujirai, K. Ogasawara, S. Matsuishi, T. Tada, H. Abe, Y. Niwa and H. Hosono, *J. Am. Chem. Soc.*, 2019, **141**, 20344.
19 K. Ooya, J. Li, K. Fukui, S. Iimura, T. Nakao, K. Ogasawara, M. Sasase, H. Abe, Y. Niwa, M. Kitano and H. Hosono, *Adv. Energy Mater.*, 2021, **11**, 2003723.
20 H. Yamashita, T. Broux, Y. Kobayashi, F. Takeiri, H. Ubukata, T. Zhu, M. A. Hayward, K. Fujii, M. Yashima, K. Shitara, A. Kuwabara, T. Murakami and H. Kageyama, *J. Am. Chem. Soc.*, 2018, **140**, 11170.
21 K. Wang, Z. Wu and D. Jiang, *Phys. Chem. Chem. Phys.*, 2022, **24**, 1496.
22 H. Kageyama, K. Hayashi, K. Maeda, J. P. Attfield, Z. Hiroi, J. M. Rondinelli and K. R. Poeppelmeier, *Nat. Commun.*, 2018, **9**, 772.
23 Y. Kobayashi, O. J. Hernandez, T. Sakaguchi, T. Yajima, T. Roisnel, Y. Tsujimoto, M. Morita, Y. Noda, Y. Mogami, A. Kitada, M. Ohkura, S. Hosokawa, Z. Li, K. Hayashi, Y. Kusano, J. E. Kim, N. Tsuji, A. Fujiwara, Y. Matsushita, K. Yoshimura, K. Takegoshi, M. Inoue, M. Takano and H. Kageyama, *Nat. Mater.*, 2012, **11**, 507.
24 T. Uchimura, F. Takeiri, K. Okamoto, T. Saito, T. Kamiyama and G. Kobayashi, *J. Mater. Chem. A*, 2021, **9**, 20371.
25 V. Petříček, M. Dušek and L. Palatinus, *Z. Kristallogr. Cryst. Mater.*, 2004, **229**, 345.
26 R. Oishi, M. Yonemura, Y. Nishimaki, S. Torii, A. Hoshikawa, T. Ishigaki, T. Morishima, K. Mori and T. Kamiyama, *Nucl. Instrum. Methods Phys. Res. A: Accel. Spectrom. Detect. Assoc. Equip.*, 2009, **600**, 94.
27 K. Aika, M. Kumasaka, T. Oma, O. Kato, H. Matsuda, N. Watanabe, K. Yamazaki, A. Ozaki and T. Onishi, *Appl. Catal.*, 1986, **28**, 57.
28 P. E. Kalita, S. V. Sinogeikin, K. E. Lipinska-Kalita, T. Hartmann, X. Ke, C. Chen and A. L. Cornelius, *J. Appl. Phys.*, 2010, **108**, 043511.
29 R. H. Buttner and E. N. Maslen, *Acta Crystallogr.*, 1992, **B48**, 764.
30 I.-K. Jeong, S. Lee, S. Jeong, C. J. Won, N. Hur and A. Llobet, *Phys. Rev. B*, 2011, **84**, 064125.
31 P. R. Arya, P. Jha and A. K. Ganguli, *J. Mater. Chem.*, 2003, **13**, 415.
32 V. F. Sears, *Neutron News*, 1992, **2**, 26.
33 B. Sreedhar, Ch. Satya Vani, D. Keerthi Devi, V. Sreeram and M. V. Basaveswara Rao, *Am. J. Mater. Sci.*, 2012, **2**, 105.
34 K. B. Park, J. H. Choi, T. W. Na, J. W. Kang, K. S. Park and H. K. Park, *Metals*, 2019, **9**, 1154.
35 K. Aika, H. Hori and A. Ozaki, *J. Catal.*, 1972, **27**, 424.
36 F. Rosowski, A. Hornung, O. Hinrichsen, D. Herein, M. Muhler and G. Ertl, *Appl. Catal., A*, 1997, **151**, 443.
37 X. Zhang, Q. Ye, B. Xu and D. He, *Catal. Lett.*, 2007, **117**, 140.
38 F. Hayashi, Y. Toda, Y. Kanie, M. Kitano, Y. Inoue, T. Yokoyama, M. Hara and H. Hosono, *Chem. Sci.*, 2013, **4**, 3124.